Hindawi
Shock and Vibration
Volume 2020, Article ID 8827333, 18 pages
https://doi.org/10.1155/2020/8827333

Research Article

Effect of Blade Outlet Angle on Radial Force of Marine Magnetic Drive Pump

Hong-li Zhang,[1] Fan-yu Kong,[1] Ai-xia Zhu,[2] Fei Zhao,[1,3] and Zhen-fa Xu[1]

[1]*Research Center of Fluid Machinery Engineering and Technology, Jiangsu University, Zhenjiang 212013, China*
[2]*Totecber (Hangzhou) Technology Co. Ltd., Hangzhou 310000, China*
[3]*School of Mechanical Technology, Wuxi Institute of Technology, Wuxi 214121, China*

Correspondence should be addressed to Hong-li Zhang; zhanghonglivip@126.com

Received 27 May 2020; Revised 4 August 2020; Accepted 26 August 2020; Published 11 September 2020

Academic Editor: Zhixiong Li

Copyright © 2020 Hong-li Zhang et al. This is an open access article distributed under the Creative Commons Attribution License, which permits unrestricted use, distribution, and reproduction in any medium, provided the original work is properly cited.

To research the effects of the blade outlet angle on the performance and the radial force of the marine pump, the unsteady numerical simulation of the four different models is carried out. The radial forces on the impeller and the blades are obtained under different flow rate conditions. The time and frequency domain characteristics of radial resultant force on the impeller and the blades are analyzed and those of the impeller torque are researched. The results show that the radial forces of the impeller and the blades increase with the increase of the blade outlet angle at the same flow rate. With the same blade outlet angle, the radial forces decrease with the increase of the flow rate. The roundness of radial force vector diagram becomes more obvious with the decrease of the blade outlet angle. The root mean square (RMS) of radial force on the blades is about 30% of that on the impeller. The main frequency of radial force on the impeller and the blades is the axial passing frequency (APF), and that of impeller torque is the blade passing frequency (BPF), and there are peaks at the blade frequency multiplier. At the same flow rate, the main frequency and maximum fluctuation amplitudes on the impeller and the blades increase with the increase of the blade outlet angle. Meanwhile, the impeller torque increases with the increase of the blade outlet angle. With the same blade outlet angle, the main frequency, maximum fluctuation amplitudes, and the impeller torque decrease with the increase of the flow rate. The amplitude difference decreases with the increase of the flow rate. The blade outlet angle has an obvious greater influence on the radial forces and fluctuation at the small flow rate. The vibration test shows that the vibration intensities of model 25 and model 35 are less than 2.5 mm/s, and the vibration intensity of model 25 is about 0.2 mm/s less than that of model 35.

1. Introduction

The marine pumps are commonly used in complex environments, which need to have the characteristics of small vibration, low noise, and high reliability. The liquid medium dynamic reaction force on the impeller in the centrifugal pump produces radial force, and the fluctuation of radial force makes the pump shaft subject to alternating stress, which results in pump vibration of different degrees.

At present, there are many research studies on the internal flow pressure fluctuation, radial force, and vibration mechanism in the centrifugal pump and pump as turbine. The reduction of noise is significant by increasing the gap between the impeller and the tongue [1]. The flow pressure fluctuates with the interaction between the tongue and the blades, the impeller gap is investigated, and the pressure around the tongue fluctuates largely [2–5]. The pressure fluctuations at the top dead centre of the volute provide a better indication than at the discharge [6]. The radial and axial distributions of the fluctuation characteristics at the gap of the pump are analyzed, and the maximum pressure fluctuation occurs at the blade front side [7]. The pressure fluctuations in the impeller inlet show more complication in part flow conditions than at the best efficiency point [8]. The sound excitation in the pump by a source of pressure oscillations positioned in the inlet is considered, and resonant acoustic excitation may occur in the pump [9]. The effect of blade trailing edge on pressure characteristics is investigated, and the rotor-stator interaction is the main factor affecting pressure pulsation [10]. The impeller trimming on the

performance of the pump as turbine is investigated, and the accuracy of computational fluid dynamics is validated [11]. The pressure fluctuations at the vanes' passages and vaneless space are predicted, and the amplitude in the high pressure side passage of the vane is lower [12]. The pressure fluctuation in the vaneless region under different guide vane states is studied; the pressure fluctuation in the vaneless region is greatly affected by the guide blade vibration [13]. The increase of radial force on the impeller lags behind the increase of impeller speed [14]. The clocking effect has great influence on the pressure fluctuation and the radial force on the impeller [15]. The front impeller wear ring has great influence on the axial force of the centrifugal pump [16]. The effects of concentric volute and multivolute geometry on the radial force of the centrifugal pump at off-design conditions are investigated, and the triple volute is the most appropriate volute geometry [17]. The effect of outlet diameter, outlet width, blade outlet angle, blade wrap angle, blade number, and blade shape of the impeller on the pump performance is analyzed, and multiparameter optimization improves pump efficiency and reduces vibration [18–21].

In addition, the time domain and frequency domain of pressure fluctuation at monitoring point on diffuser and outlet elbow are analyzed in mixed flow pump, and the pressure fluctuation peak decreases gradually with the increase of the flow rate [22]. The radial force on principal axis is compared between mixed flow pump as turbine with symmetrical and unsymmetrical tip clearances; the main frequency of radial force of symmetrical tip clearance is related to the blade number [23]. The identification of the relationship between pressure fluctuation and vibration is analyzed, the amplitudes may be overvalued when the sampling time is short [24]. The stall cell number and circumferential propagation velocity under stall condition are calculated according to the pressure fluctuation characteristics [25]. The increase of tip leakage flow increases the energy loss in the impeller [26]. The increase of the end clearance leads to the decrease of the head and efficiency in the submersible pump [27]. The simulation can accurately predict the bubble morphology compared with the experimental result in the pump multiphase transient [28]. The application of the transfer pump in biomass cycle combustion system simulation is analyzed [29]. At small flow rate, the pump flow is very unstable with significant backflow in a centrifugal slurry pump. With the increase in particle concentration, the flow resistance increases and the backflow increases [30].

The blade outlet angle of research on the influence of radial force in the centrifugal pump is less, so the effect of different blade outlet angles on radial force of the marine pump is necessary for research. The internal flow field in the magnetic drive pump is analyzed with the numerical calculation method. The radial force on the impeller and the blades, and impeller torque at various flow rates are obtained. The time domain and frequency domain characteristics of radial force and impeller torque are analyzed. The hydraulic performance and vibration tests are carried out on the real pump, which provided a reference for further research on radial force and vibration of the pump.

2. Example of Marine Magnetic Drive Pump

2.1. Main Design Parameters. The marine magnetic drive pump is researched as an object; its design parameters are rated flow $Q = 140\,\mathrm{m}^3/\mathrm{h}$, head $H = 40\,\mathrm{m}$, rotation $n = 2950\,\mathrm{r/min}$, and specific speed $n_s = 133.5$. The main geometric parameters of the pump are shown in Table 1. The impeller structure is an enclosed impeller with forward curved blades. The four groups of blade outlet angles are selected, which are 25°, 30°, 35°, and 40°. The corresponding pump models are called model 25, model 30, model 35, and model 40, respectively.

2.2. The Main Structure. The structure of the magnetic drive pump is shown in Figure 1. The pump cooling mode adopted water cooling instead of the traditional air cooling mode, which can effectively reduce the overall noise of the pump unit. The pump is designed as a double volute structure to reduce the radial force and it is installed vertically.

3. Numerical Calculation of Full-Flow Field

3.1. Full-Flow Field Model. The cavities between the front shroud, the back shroud, and the volute are taken into account in the modeling. The flow field with minimal gaps between the impeller rings and the volute can also be effectively captured. The model includes inlet pipe, outlet pipe, volute, impeller, front cavity, back cavity, and balance holes. Therefore, the full-flow field numerical simulation analysis is adopted, and the calculation results include volume loss and disc friction loss.

The structured hexahedral mesh of components in the model is generated with ICEM software. It can be better divided as the small area of impeller rings and tongue. The mesh independence of the model is checked, and the mesh is finally exported in cfx5 format. The impeller mesh and schematic diagram of the pump is shown in Figure 2.

The mesh independence of the model is studied with model 35 as an example. The relation curve between the head of the pump and the mesh number under the design flow rate is shown in Figure 3. The head gradually increases with the mesh number; when the mesh number is more than 1.58 million, the variation range of head is less than 0.11%. Therefore, it is more appropriate for the mesh number to be more than 1.58 million, and the mesh number of model 35 is 1587 850.

3.2. Boundary Setting and Turbulence Model. The steady and unsteady flow fields inside the pump are calculated with Ansys CFX. The inlet of the pump model is set as static pressure inlet and the outlet as mass flow outlet. The wall roughness of the pump is set at 50 μm, and the convergence standard is 10^{-5}.

Model 35 is analyzed by using the standard k-ε, RNG k-ε, k-ω, and *SST* turbulence models. The simulation head, efficiency, and shaft power of the pump are obtained. The simulation values with four different turbulence models are compared with the pump hydraulic test value. The diagram

Table 1: Main geometric parameters of the designed magnetic drive pump.

	Parameters	Value
	Impeller outlet diameter D_2 (mm)	102
	Impeller outlet diameter D_2 (mm)	194
	Impeller outlet width b_2 (mm)	21.6
	Impeller hub diameter dh (mm)	48
	Blade inlet angle $\beta_1/(^\circ)$	15–20
Impeller 25	Blade outlet angle $\beta_2/(^\circ)$	25
Impeller 30	Blade outlet angle $\beta_2/(^\circ)$	30
Impeller 35	Blade outlet angle $\beta_2/(^\circ)$	35
Impeller 40	Blade outlet angle $\beta_2/(^\circ)$	40
	Blade wrap angle $\Phi/(^\circ)$	106
	Blade number Z	6
	Volute base circle diameter D_3 (mm)	210
	Tongue angle $\varphi/(^\circ)$	32.7

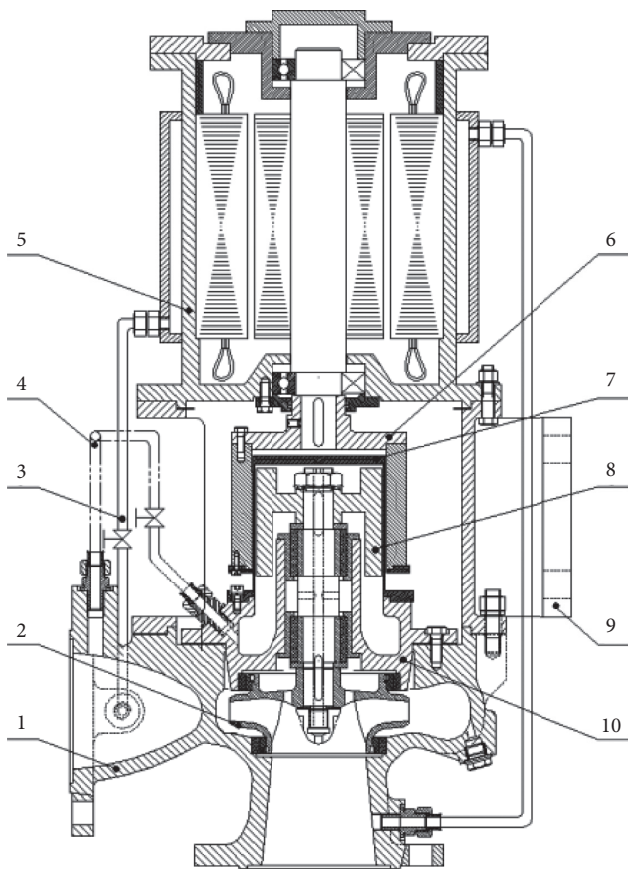

Figure 1: Structure of the magnetic drive pump. 1. Volute. 2. Impeller. 3. Motor cooling pipe. 4. Pump cooling pipe. 5. Motor. 6. Outside magnetic rotor. 7. Isolator. 8. Inside magnetic rotor. 9. Connecting body. 10. Guide bearing.

of simulation values with different turbulence models are shown in Figure 4. It can be seen from Figure 4 that the simulation values with the RNG k-ε are more consistent with the pump test value on the head, efficiency, and shaft power under full working conditions. Therefore, the RNG k-ε turbulence model is selected in the subsequent pump simulation.

The RNG k-ε adds a condition to the ε equation of standard k-ε model and provides an analytic formula of flow viscosity with low Reynolds number. It can improve the calculation accuracy, and the transport equations for k and ε are as follows:

$$\frac{\partial(\rho k)}{\partial t}+\frac{\partial(\rho k u i)}{\partial x\, i}=\frac{\partial}{\partial x\, j}\left[\left(\mu+\frac{\mu_t}{\sigma_k}\right)\frac{\partial k}{\partial x\, j}\right]+G_k-\rho\varepsilon,$$

$$\frac{\partial(\rho\varepsilon)}{\partial t}+\frac{\partial(\rho\varepsilon u i)}{\partial x\, i}=\frac{\partial}{\partial x\, j}\left[\left(\mu+\frac{\mu_t}{\sigma_\varepsilon}\right)\frac{\partial \varepsilon}{\partial x\, j}\right]+C_{1\varepsilon}^{*}\frac{\varepsilon}{k}G_k-C_{2\varepsilon}\frac{\rho\varepsilon^2}{k}, \quad (1)$$

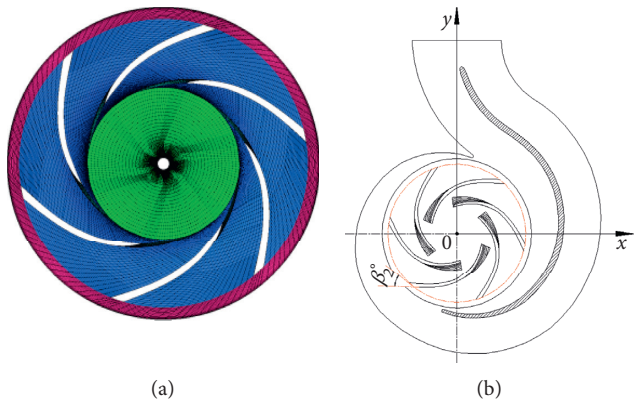

Figure 2: (a) Impeller mesh and (b) schematic diagram of pump.

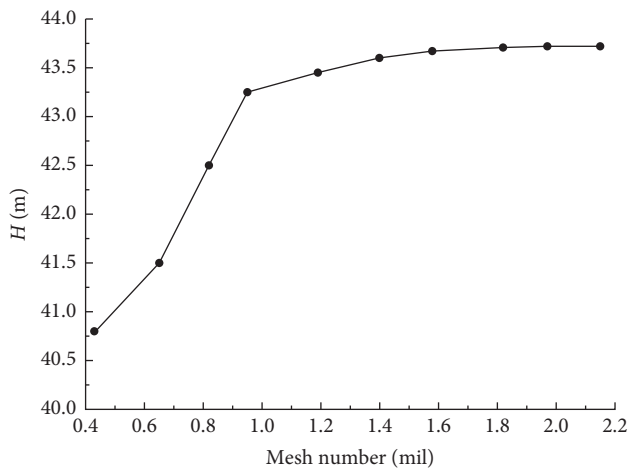

Figure 3: Variation of head with mesh number in model 35.

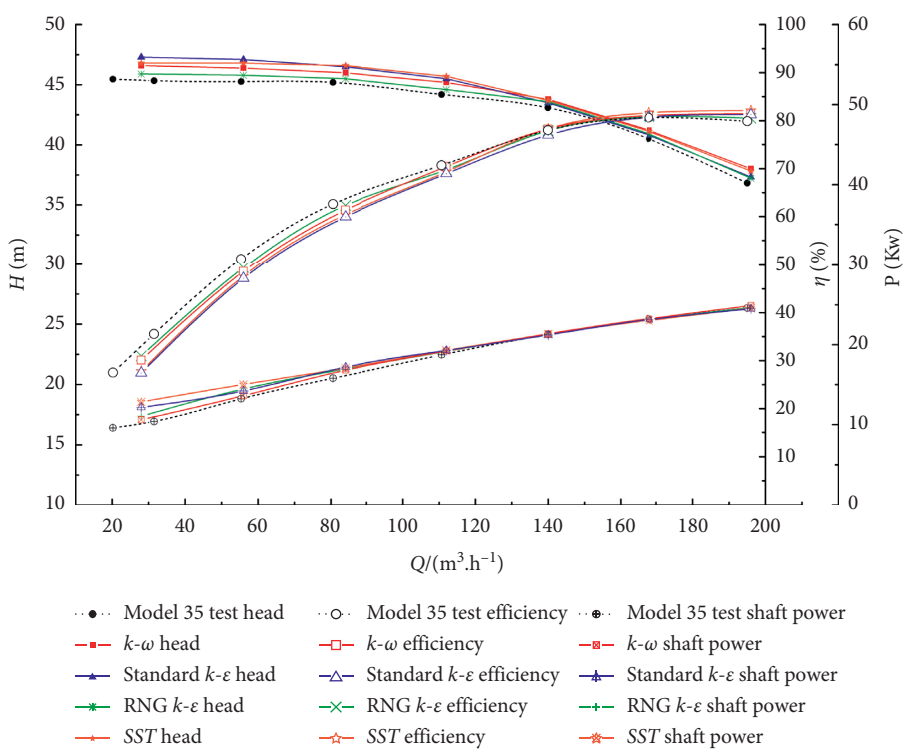

Figure 4: Diagram of simulation values with different turbulence models.

where $\mu_t = C_\mu(\rho k^2/\varepsilon)$, $G_k = \mu_t((\partial u_i/\partial x_j) + (\partial u_j/\partial x_i))\partial u_i/\partial x_j$, $C_{1\varepsilon}^* = C_{1\varepsilon} - \eta(1 - (\eta/\eta_0))/1 + \beta\eta^3, \eta = (2E_{ij} \cdot E_{ij})^{1/2}k/\varepsilon$, $E_{ij} = 1/2((\partial u_i/\partial x_j) + (\partial u_j/\partial x_i))$, $\sigma_k = \sigma_\varepsilon = 0.178$, $C_\mu = 0.0845$, $\eta_0 = 4.377$, $\beta = 0.012$, $C_{1\varepsilon} = 1.42$, and $C_{2\varepsilon} = 1.68$.

The frozen rotor interface is set for steady calculation, while the unsteady calculation uses the transient rotor interface in the CFX. The results of steady analysis are used as the initial conditions for unsteady calculation. In the unsteady calculation, the time step setting is considered as follows. If the time of 2° rotation of the impeller is taken as the time step, the sampling points per revolution are 180, and the sampling resolution is slightly lower. Meanwhile, considering the pump speed and the resources of the computer, the time of 1° rotation of the impeller is set as the time step, which is 5.649×10^{-5}·s. When the transient analysis runs for 15 revolutions, the flow field presents periodic change and that is stable. The result of the 15th revolution is taken as the analysis. The time domain and frequency domain analysis of radial forces on the impeller and blades and impeller torque are carried out.

4. Results and Discussion

4.1. Radial Force Analysis on the Impeller. The y plus contour map can effectively estimate whether the boundary layer division of the pump model is reasonable, and the range of turbulent boundary layer can be determined according to the y plus contour map of the blade surface. The y plus on front and back sides of blade is shown in Figure 5. It can be seen from Figure 5 that the y plus on the back and front sides of blade is less than 400. It can be explained that the boundary layer thickness setting is more reasonable in the pump model, and the simulation results are reliable. The minimum value of y plus on the back of the blade is 5.6 and the maximum value is 263.5. At the same time, the minimum value of y plus on the front of the blade is 3.6 and the maximum value is 373.5. According to the thickness of the grid, the turbulence model automatically solves the viscous bottom layer and the logarithmic layer.

The vector diagram of radial force on the impeller under different flow rate conditions is shown in Figure 6. It can be seen from Figure 6 that the magnitude and direction of the radial force on the impeller are changing at all times. At the same flow rate, the radial force on the impeller increases with the increase of the blade outlet angle. At the flow rate of 0.8Q, the uniformity of radial force difference among the four models is poor in different quadrants. The change of the flow angle at the blade outlet leads to the mismatch with the helical angle of the tongue, which intensifies the rotor-stator interaction between the impeller and the volute.

With the same blade outlet angle, the radial force on the impeller decreases with the increase of the flow rate. The radial force vector diagram gradually tends to be circular and concentric, and the roundness becomes more obvious with the decrease of the blade outlet angle. At each flow rate, the radial force vector diagrams in the four groups of models present obvious sidelobes. The number of sidelobes is 6 and the same as the number of leaves, which is mainly caused by the rotor and stator interference generated by the blade passing through the tongue region. It is shown that the fluctuation frequency of radial force is related to the number of blades and mainly to the blade frequency.

The time domain of radial resultant force on the impeller under different flow rate conditions is shown in Figure 7. It can be seen that, at each flow rate, the overall trend of the radial resultant force on the impeller fluctuates periodically with time, and there are 6 peaks and troughs. In the same model, there are also small fluctuations between adjacent sampling points. It indicates that pressure pulsation influences the radial force at all times during the pump operation.

$$F(\omega) = \int_{-\infty}^{\infty} f(t)e^{-\omega t}d_t. \quad (2)$$

At the flow rate of 0.8Q, the radial resultant force has a large variation amplitude, and the variation amplitude of the resultant force obviously decreases with the increase of the flow rate. At the same flow rate, the radial resultant force increases with the increase of the blade outlet angle. The main reason is that the absolute velocity at the impeller outlet increases as the blade outlet angle increases, and the dynamic pressure increases. The increase of the pressure will lead to the increase of the radial force.

The formula of Fast Fourier Transform (FFT) is as shown formula (2), where $f(t)$ is time domain function and $F(\omega)$ is continuous frequency spectrum. The time domain values are converted to frequency domain values by FFT. By comparing the relation between the amplitude and frequency of radial resultant force at different flow rates, the degree of fluctuation can be expressed more accurately. The frequency domain of radial resultant force on the impeller under different flow rate conditions is shown in Figure 8. It can be seen that, at each flow rate, the main frequency of the radial resultant force fluctuation on the impeller is the APF. There are peaks at the BPF and blade frequency multiplier, and the peak value gradually decreases.

The amplitude of frequency domain and maximum fluctuation of radial resultant force on the impeller are shown in Table 2. The maximum fluctuation amplitude value in the table is calculated by formula $(N_{\max} - N_{\min})/\rho H \times 100$, where $N_{\max}$ and $N_{\min}$ are, respectively, the maximum and minimum values of the radial resultant force on the impeller (N) and ρ is density (Kg/m^3). The amplitude difference is the difference between the maximum and the minimum values of the maximum fluctuation amplitude under the same flow rate condition. The influence degree of different blade outlet angles on the radial resultant force can be seen from amplitude difference value.

As can be seen from Figure 8 and Table 2, at the same flow rate, the main frequency and the maximum fluctuation amplitudes of the radial resultant force on the impeller increase with the increase of the blade outlet angle. It shows that the blade outlet angle is small, which has little influence on the radial force of the impeller. That is mainly due to the reason of rotor-stator interference in the pump. For the same blade outlet angle, the main frequency and the maximum fluctuation amplitudes decrease with the increase of the flow rate.

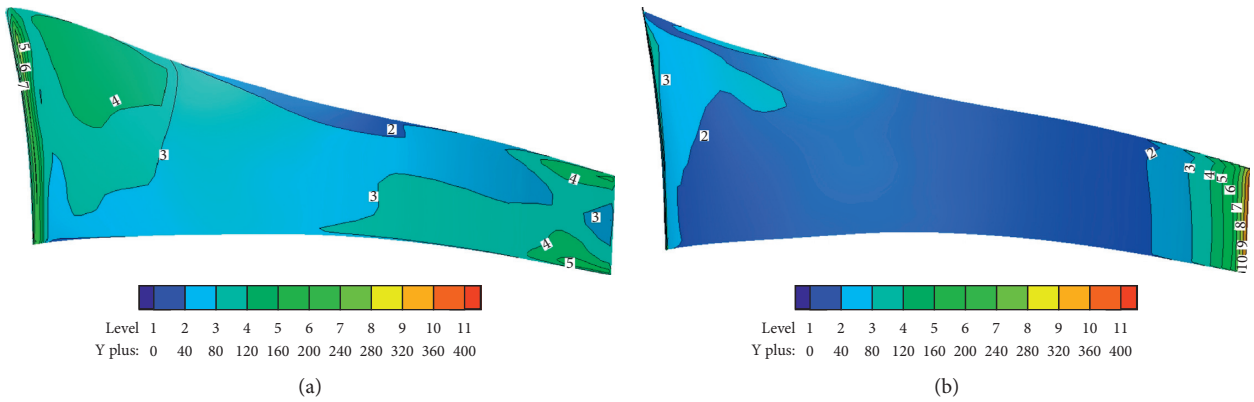

Figure 5: y plus on front and back sides of the blade.

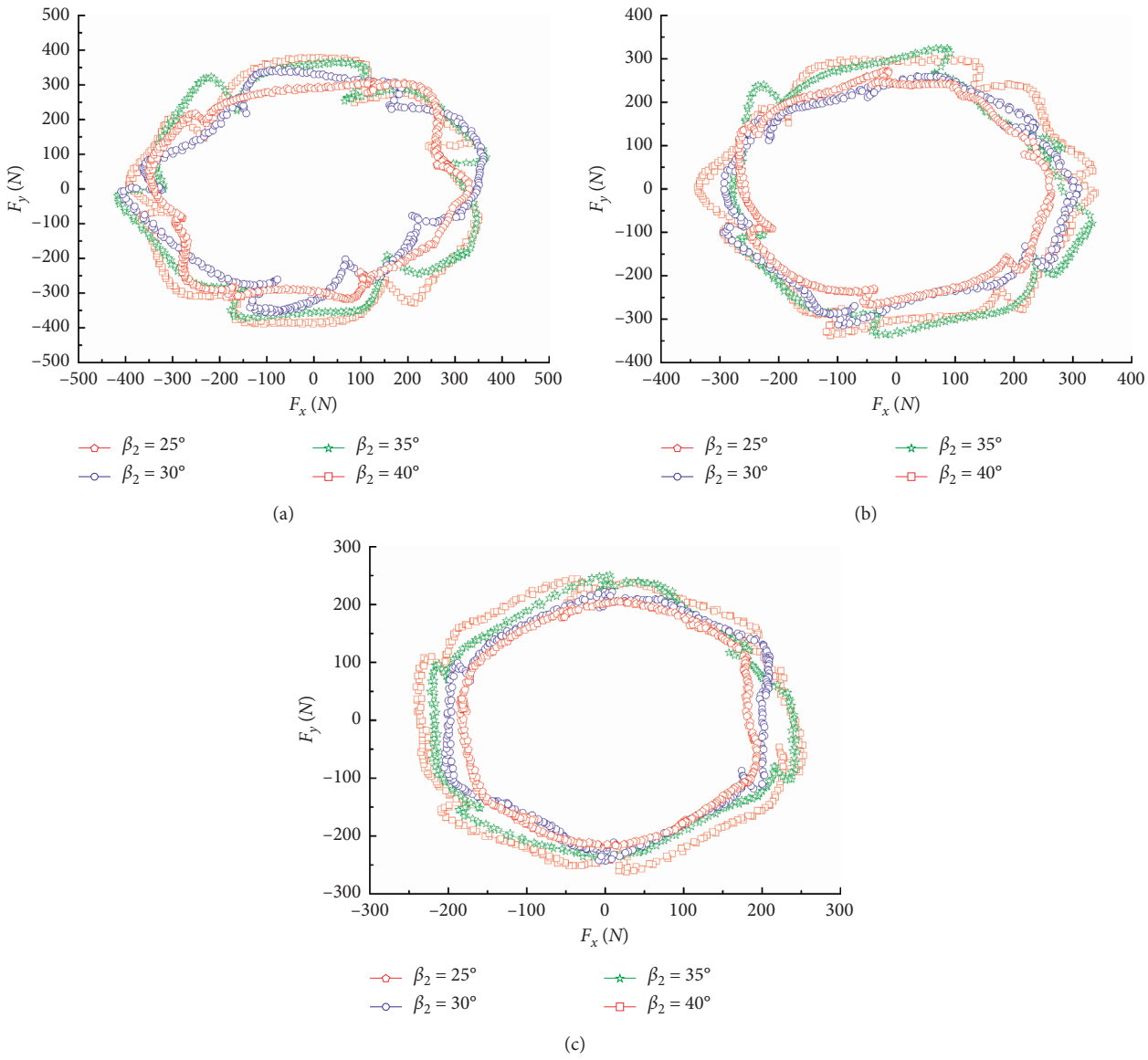

Figure 6: Vector diagram of radial force on the impeller under different flow rate conditions. (a) 0.8Q. (b) 1.0Q (c) 1.2Q.

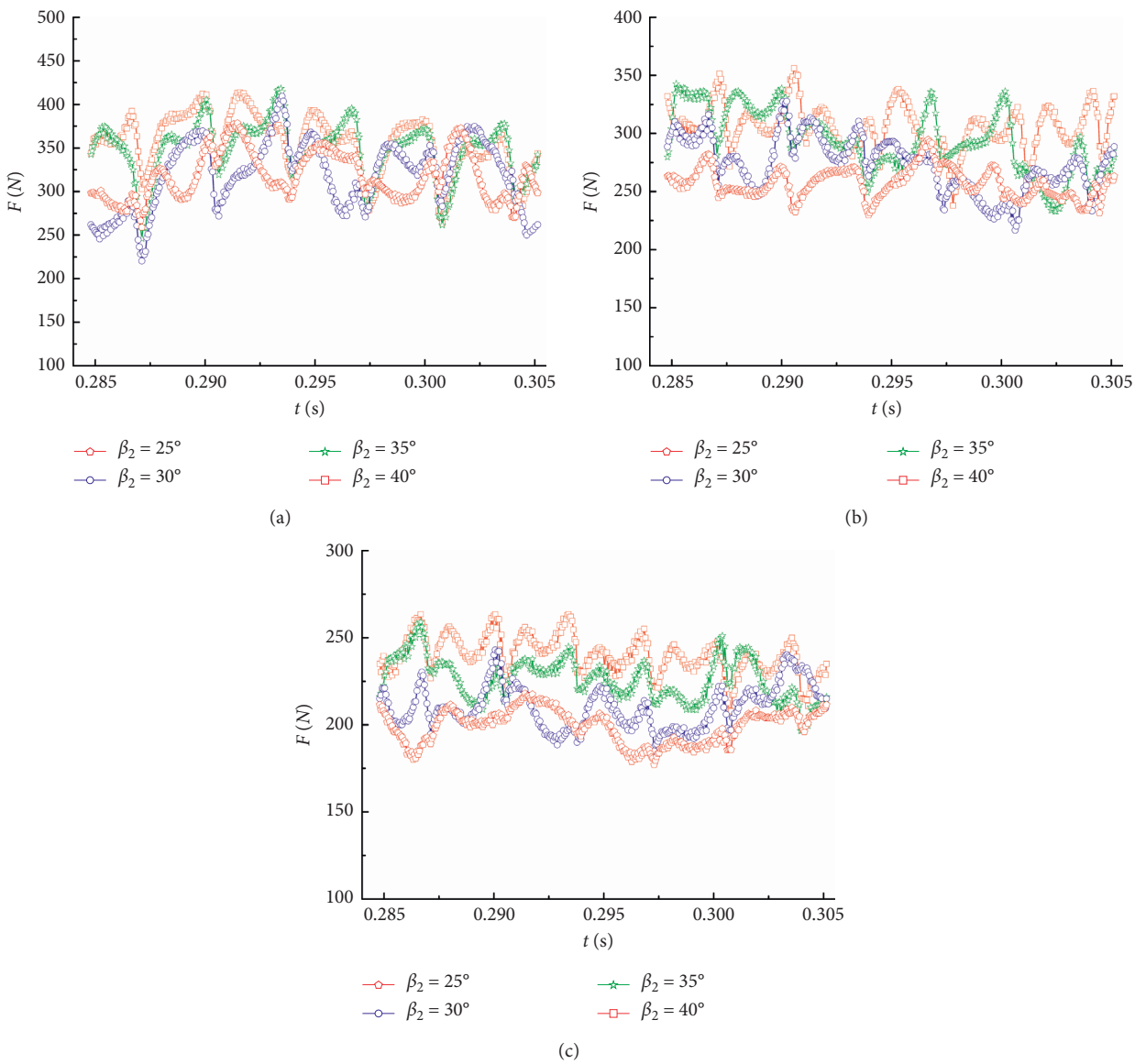

Figure 7: Time domain of radial resultant force on the impeller under different flow rate conditions. (a) 0.8Q. (b) 1.0Q. (c) 1.2Q.

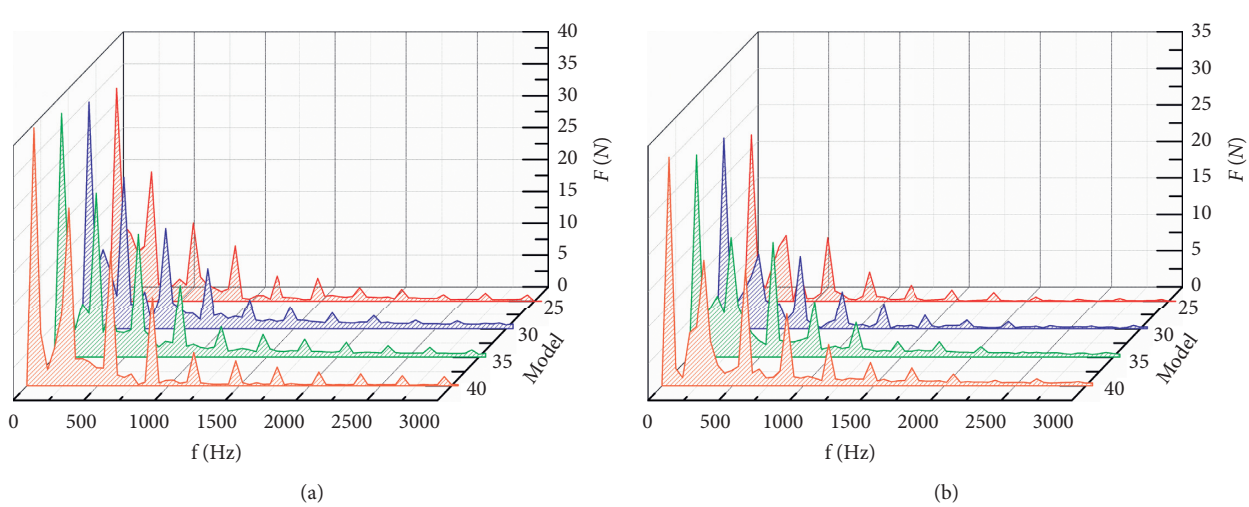

Figure 8: Continued.

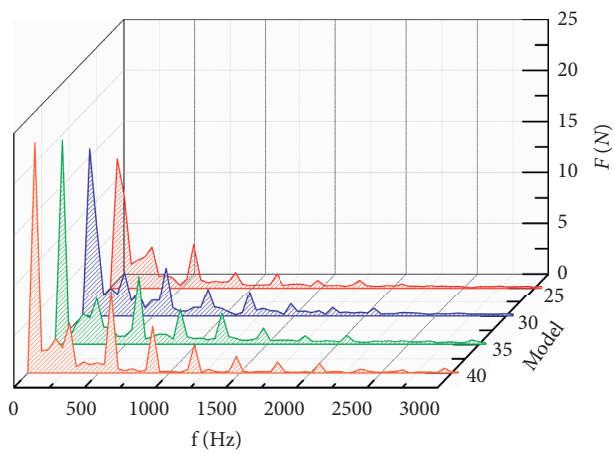

(c)

Figure 8: Frequency domain of radial resultant force on the impeller under different flow rate conditions. (a) 0.8Q. (b) 1.0Q. (c) 1.2Q.

Table 2: Amplitude of frequency domain and maximum fluctuation of radial resultant force on the impeller.

Flow	Model	Main frequency amplitude (N)	Maximum fluctuation amplitude (%)	Amplitude difference (%)
0.8Q	25	33.4	0.4153	0.1716
	30	35.7	0.5173	
	35	38.4	0.5401	
	40	40.6	0.5869	
1.0Q	25	22.8	0.2461	0.1529
	30	26.3	0.2757	
	35	27.9	0.2993	
	40	31.5	0.3990	
1.2Q	25	12.7	0.1405	0.1308
	30	16.5	0.1684	
	35	20.1	0.2023	
	40	22.6	0.2713	

The amplitude difference decreases with the increase of the flow rate. It indicates that the blade outlet angle has the more significant effect on the radial force and fluctuation on the impeller at the small flow rate. The main reason is that the impeller runner is designed according to the hydraulic model under the design flow rate condition. When the flow rate is small, the back flow and flow separation appear in the internal pump so that the radial force on the impeller is not in balance, thus increasing the radial force on the impeller and reducing the hydraulic efficiency.

4.2. Radial Force Analysis on the Blades. The pressure contour maps on the front side of blades with different blade outlet angles are shown in Figure 9. It can be seen from Figure 9 that the pressure values of the six blades are not completely the same, and there is obvious difference. The pump internal flow is complex; the interaction between the volute and the impeller exists in the operation of centrifugal pump. With the same blade outlet angle, the pressure on the blade surface decreases with the increase of flow. With the same flow rate, the pressure on blade surface increases with the increase of blade outlet angle. When the flow rate is 1.2Q, and the blade outlet angle is 25°, the minimum pressure of the blade is shown in Figure 9(c). When the flow rate is 0.8Q and the blade outlet angle is 40°, the maximum pressure of the blade is shown in Figure 9(j). The influence of the blade outlet angle on blade surface pressure is consistent with the variation trend of radial force in Figures 7 and 10.

The vector diagram of radial force on the blades under different flow rate conditions is shown in Figure 11. It can be seen from Figures 6 and 11 that the radial force on the blades and the impeller has the same change trend, and the radial force on the blades decreases with the increase of the flow rate. Under the small flow rate and design flow rate conditions, the radial force difference on the blades between the four models is less uniform in different quadrants.

At the flow rate of 1.2Q, the difference becomes more uniform. There are 6 obvious sidelobes in the radial force vector diagram on the blades at different flow rates, and the radial force on the blades is significantly smaller than that on the impeller. That is mainly the influence of radial force on the front and back shrouds of the impeller is more significant.

The time domain of radial resultant force on the blades under different flow rate conditions is shown in Figure 10.

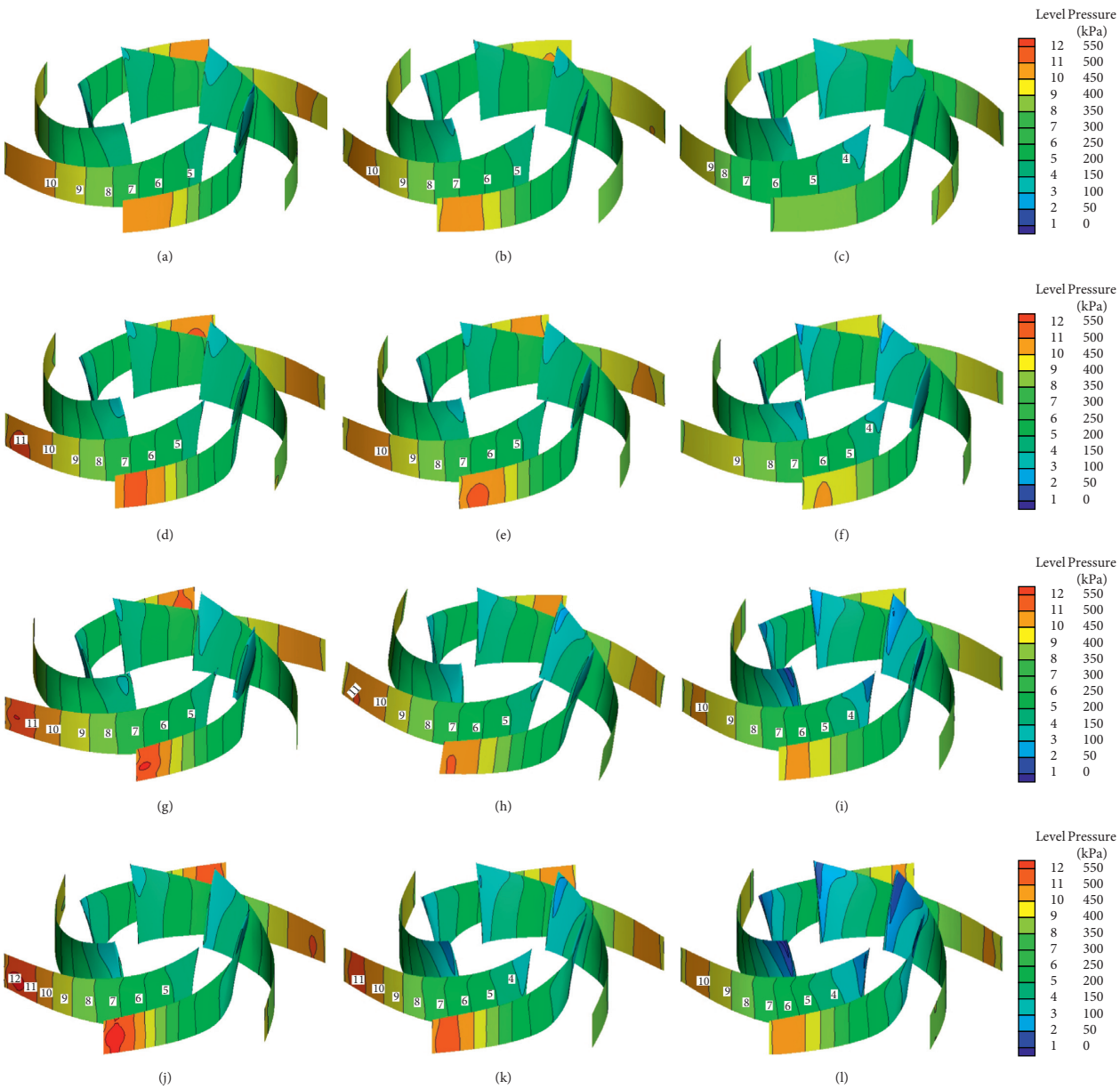

Figure 9: Pressure contour maps on the front side of blades with different blade outlet angles. (a) 0.8Q ($\beta_2 = 25^\circ$). (b) 1.0Q ($\beta_2 = 25^\circ$). (c) 1.2Q ($\beta_2 = 25^\circ$). (d) 0.8Q ($\beta_2 = 30^\circ$). (e) 1.0Q ($\beta_2 = 30^\circ$). (f) 1.2Q ($\beta_2 = 30^\circ$). (g) 0.8Q ($\beta_2 = 35^\circ$). (h) 1.0Q ($\beta_2 = 35^\circ$). (i) 1.2Q ($\beta_2 = 35^\circ$). (j) 0.8Q ($\beta_2 = 40^\circ$). (k) 1.0Q ($\beta_2 = 40^\circ$). (l) 1.2Q ($\beta_2 = 40^\circ$).

The RMS of the radial resultant forces on the impeller and the blades are shown in Table 3. It can be seen from Figures 7 and 10 that the radial resultant force on the impeller and the blades has the same variation trend at each flow rates and shows periodic fluctuations with time. Meanwhile, there are 6 peaks and troughs.

F_i is the RMS of radial force on the impeller and F_b is the RMS of radial force on the blades in Table 3. ΔF is the difference between the maximum and minimum values of the RMS of radial forces on the impeller and the blades at the same flow rate. As can be seen from Table 3, at the same flow rate, the RMS of radial forces on the impeller and the blades increases with the increase of the blade outlet angle. With the same blade outlet angle, the RMS of radial forces on the impeller and the blades decrease with the increase of flow. The impeller and blades ΔF values decrease with the increase of the flow rate. It is shown that the influences of the blade outlet angle on the radial forces are greater at small flow rate than at large flow rate. The RMS of the radial resultant force on the blades is about 27%–33% of that on the impeller, which is mainly distributed around 30%.

The frequency domain of radial resultant force on the blades under different flow rate conditions is shown in Figure 12. It can be seen that the main frequency of the radial resultant force on the blades is the APF at each flow rate. There are peaks at the BPF and blade frequency multiplier, and the peak value gradually decreases.

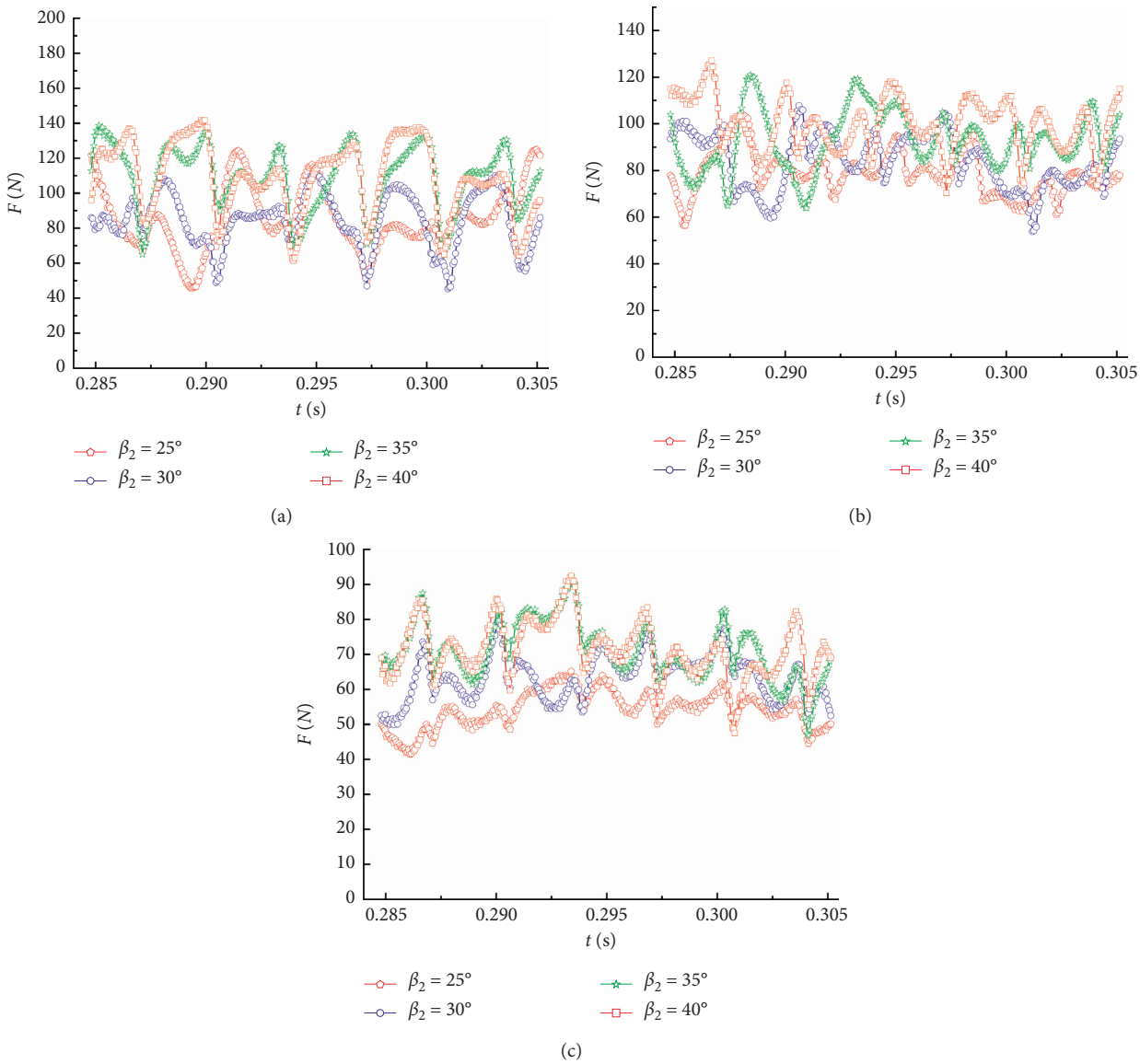

Figure 10: Time domain of radial resultant force on the blades under different flow rate conditions. (a) 0.8Q. (b) 1.0Q. (c) 1.2Q.

As can be seen from Figure 12 and Table 4, the main frequency, the maximum fluctuation amplitude, and the amplitude difference of the radial resultant force on the blades decrease gradually with the increase of the flow rate. At the same flow rate, the main frequency and the maximum fluctuation amplitudes increase with the increase of the blade outlet angle.

As can be seen from Table 4, with the same blade outlet angle, the main frequency and the maximum fluctuation amplitudes on the blades decrease with the increase of flow rate, that is, the same tendency with those on the impeller. The main frequency, the maximum fluctuation amplitude, and the amplitude difference on the blades are smaller than those on the impeller. The impeller is an enclosed structure; it has the front and back shrouds with balance holes. The radial forces of the front and back shrouds are relatively large, and we need to pay attention to them in the future research.

4.3. Impeller Torque Analysis. The time domain of torque on the impeller under different flow rate conditions is shown in Figure 13. The frequency domain of torque on the impeller under different flow rate conditions is shown in Figure 14. It can be seen from Figure 13 that the impeller torque fluctuates periodically with time at each flow rates, and there are 6 peaks and troughs with strong regularity. That is mainly caused by the rotor-stator interference between the blade and the tongue when the impeller is running in the volute. When the blade outlet angle is the same, the torque difference value after each blade passing gradually decreases with the increase of flow. The trend of the impeller torque is the same with the radial force on the impeller and the blades. While other pump parameters remain unchanged, the pump head and the impeller torque increase with the blade outlet angle increase. With the increase of the flow rate, the torque difference between four groups of models also increases. As can be seen from Figure 14, the main frequency of impeller

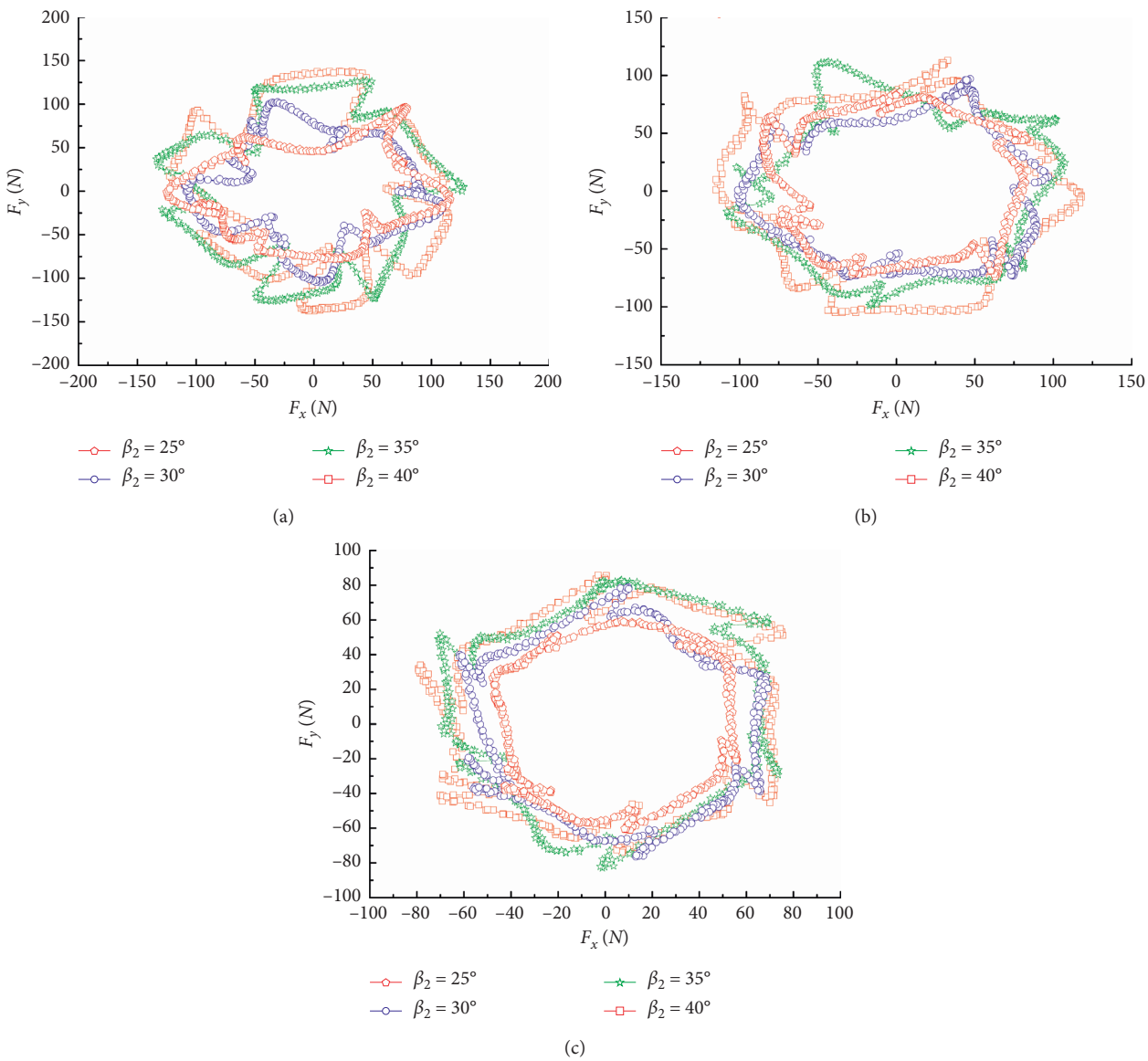

Figure 11: Vector diagram of radial force on the blades under different flow rate conditions. (a) 0.8Q. (b) 1.0Q. (c) 1.2Q.

torque fluctuation is the BPF at each flow rate. There are peaks at blade frequency multiplier, and the peak value gradually decreases.

The main frequency amplitude and maximum fluctuation amplitude of the impeller torque are shown in Table 5. The maximum fluctuation amplitude is calculated by formula $(T_{\max} - T_{\min})/\rho H \times 100$, where $T_{\max}$ and $T_{\min}$ are, respectively, the maximum and minimum values of the impeller torque (N·m).

As can be seen from Figure 14 and Table 5, at the same flow rate, the main frequency amplitude and maximum fluctuation amplitude of impeller torque increase with the increase of the blade outlet angle. The main frequency, the maximum fluctuation amplitude, and the amplitude difference decrease as the flow increases. It indicates that, under the small flow rate condition, the blade outlet angle has a slightly greater influence on the impeller torque fluctuation than under other flow rate conditions.

5. Performance Prediction and Test Verification

5.1. Hydraulic Performance Prediction and Test. Numerical analysis is carried out on four groups of models to obtain the external characteristic curve. Taking the pump head and efficiency into consideration, model 35 is selected as the experimental prototype to verify the hydraulic performance, which is measured on the closed pump test system. The external characteristic curves of the marine magnetic drive pump test and simulation are shown in Figure 15.

Table 3: RMS of radial resultant forces on the impeller and the blades.

Flow	Model	F_i (N)	F_b (N)	$F_b/F_i \times 100$
0.8Q	25	309.1	84.5	27.3
	30	321.9	86.9	27.0
	35	349.1	108.5	31.1
	40	356.6	110.6	31.0
ΔF	—	47.5	26.1	—
1.0Q	25	261.4	79.0	30.2
	30	274.3	84.8	30.9
	35	295.2	93.5	31.7
	40	305.6	100.4	32.8
ΔF	—	44.2	21.4	—
1.2Q	25	199.2	54.4	27.3
	30	210.4	63.7	30.3
	35	226.3	70.5	31.2
	40	239.9	71.6	29.8
ΔF	—	40.7	17.2	—

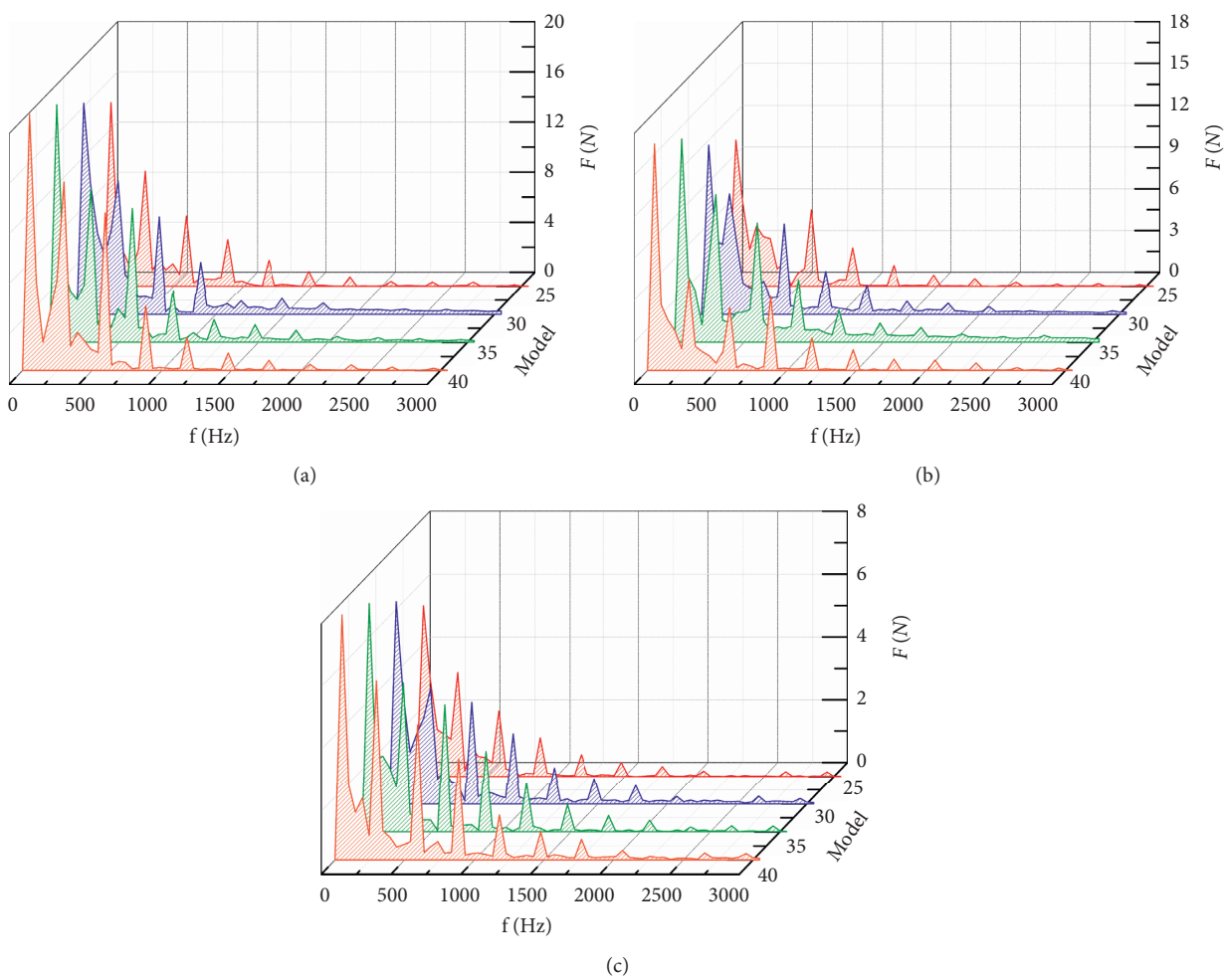

Figure 12: Frequency domain of radial resultant force on the blades under different flow rate conditions. (a) 0.8Q. (b) 1.0Q. (c) 1.2Q.

It can be seen that the simulation results of model 35 are in great agreement with the trend of the head, efficiency, and shaft power curves of the test results. Under the design flow rate condition, the simulation precision of the pump head is controlled within 1.2%, which indicates that the model can accurately simulate and predict the

Table 4: Amplitude of frequency domain and maximum fluctuation of radial resultant force on the blades.

Flow	Model	Main frequency amplitude (N)	Maximum fluctuation amplitude (%)	Amplitude difference (%)
0.8Q	25	14.7	0.1890	0.0657
	30	16.8	0.2065	
	35	18.9	0.2346	
	40	20.4	0.2547	
1.0Q	25	10.5	0.1680	0.0562
	30	12.2	0.1346	
	35	14.6	0.1631	
	40	16.3	0.2242	
1.2Q	25	5.4	0.0623	0.0445
	30	6.5	0.0910	
	35	7.3	0.0986	
	40	7.9	0.1068	

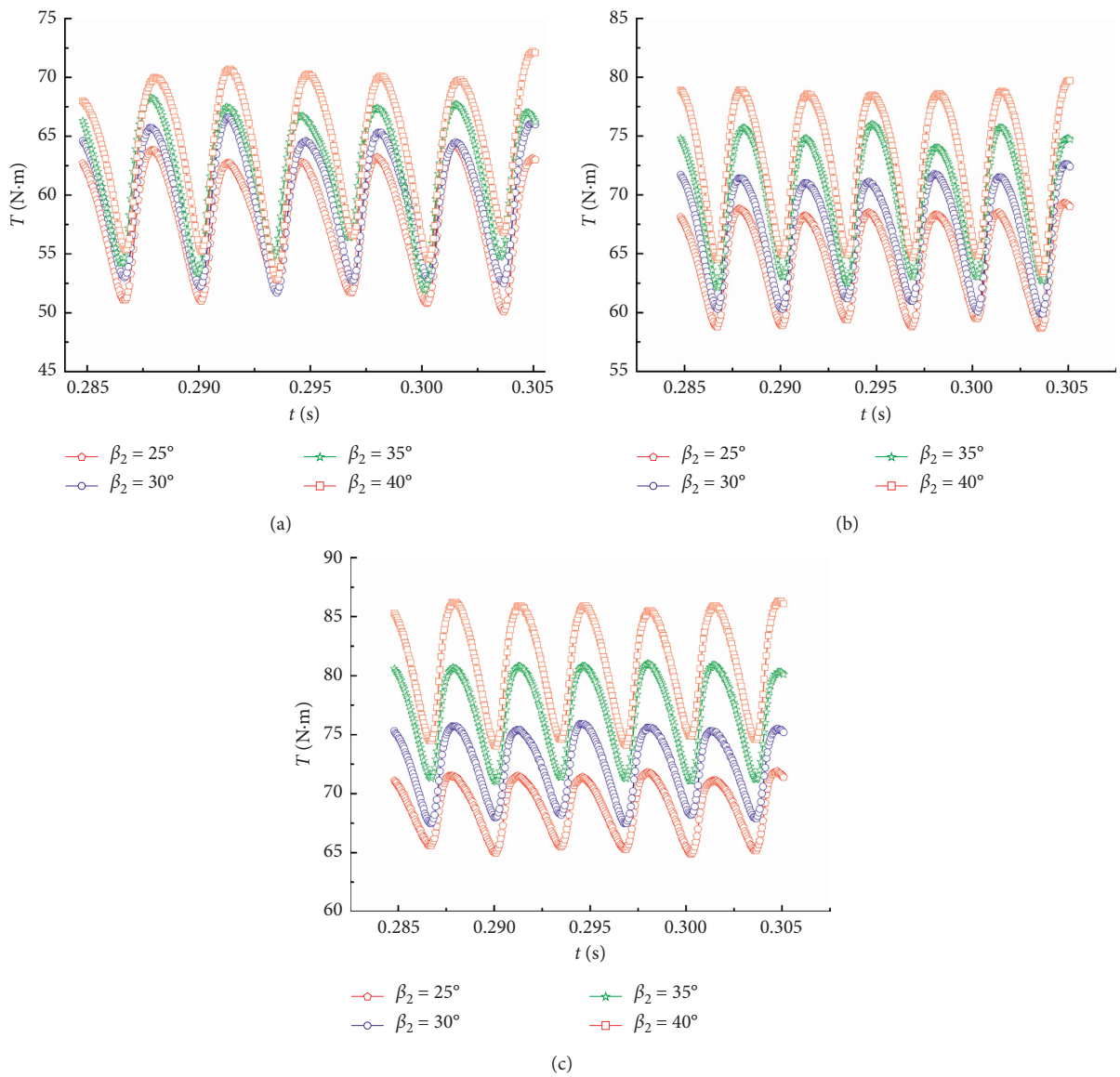

Figure 13: Time domain of torque on the impeller under different flow rate conditions. (a) 0.8Q. (b) 1.0Q. (c) 1.2Q.

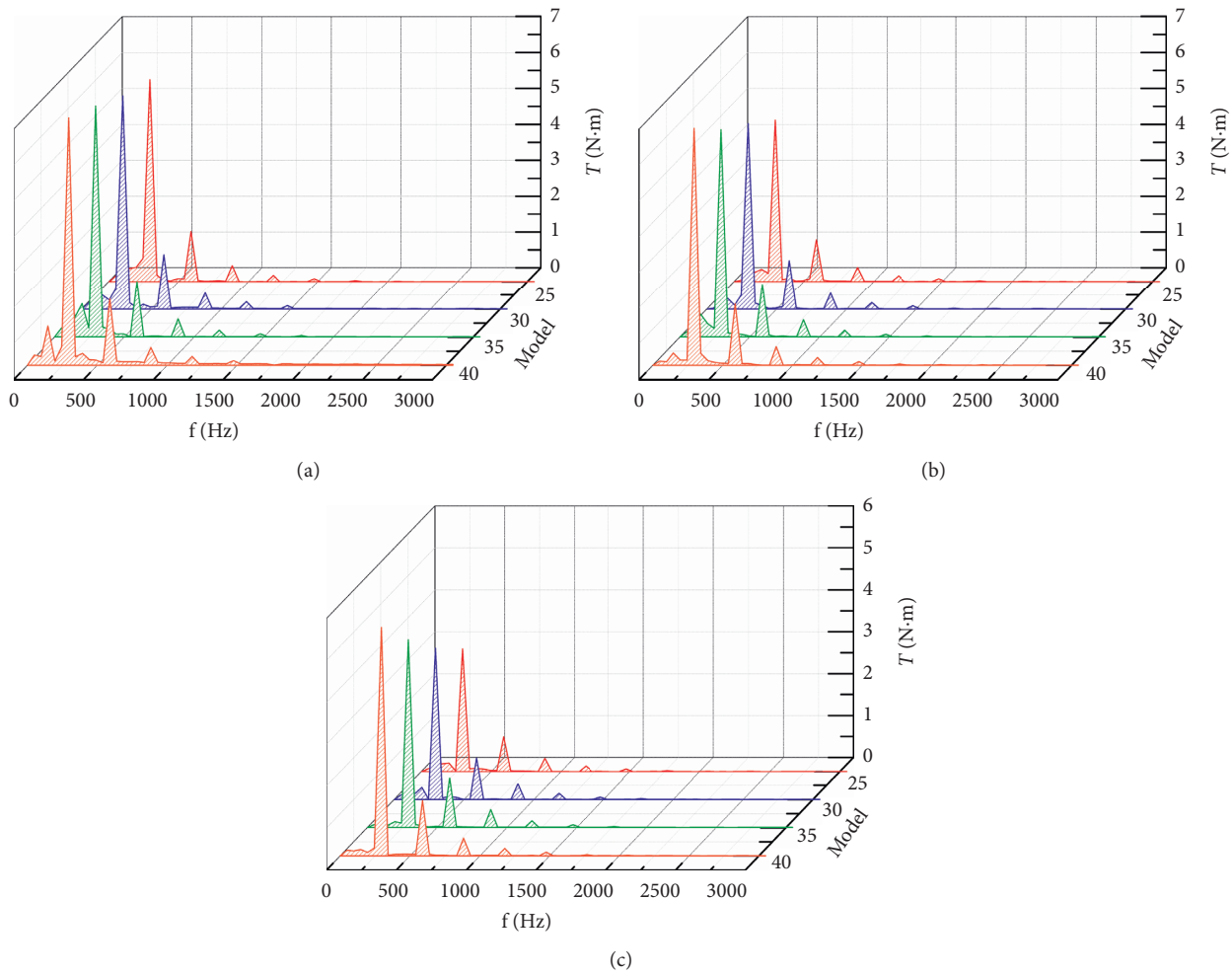

Figure 14: Frequency domain of torque on the impeller under different flow rate conditions. (a) 0.8Q. (b) 1.0Q. (c) 1.2Q.

Table 5: Amplitude of frequency domain and maximum fluctuation of torque on the impeller.

Flow	Model	Main frequency amplitude (N)	Maximum fluctuation amplitude (%)	Amplitude difference (%)
0.8Q	25	5.63	0.0309	0.0124
	30	5.96	0.0347	
	35	6.47	0.0374	
	40	6.92	0.0433	
1.0Q	25	4.51	0.0258	0.0112
	30	5.20	0.0300	
	35	5.80	0.0319	
	40	6.63	0.0370	
1.2Q	25	2.93	0.0184	0.0108
	30	3.61	0.0213	
	35	4.49	0.0244	
	40	5.45	0.0292	

pump hydraulic performance. By comparing the simulation results of four different blade outlet angles, it can be seen that the head is obviously improved, and the efficiency has a decreasing trend with the increase of the blade outlet angle. The main reason is that the impeller runner gets shorter with the increase of the blade outlet angle. The medium diffusion in the impeller runner gets larger, and the fluid hydraulic loss increases. Meanwhile, the hydraulic efficiency of the pump decreases at small flow rate.

5.2. Vibration Verification Test. According to ISO 10816 vibration evaluation standard for rotating machinery, the vibration test is carried out for pump prototypes with blade outlet angles of 25° and 35°. Considering the

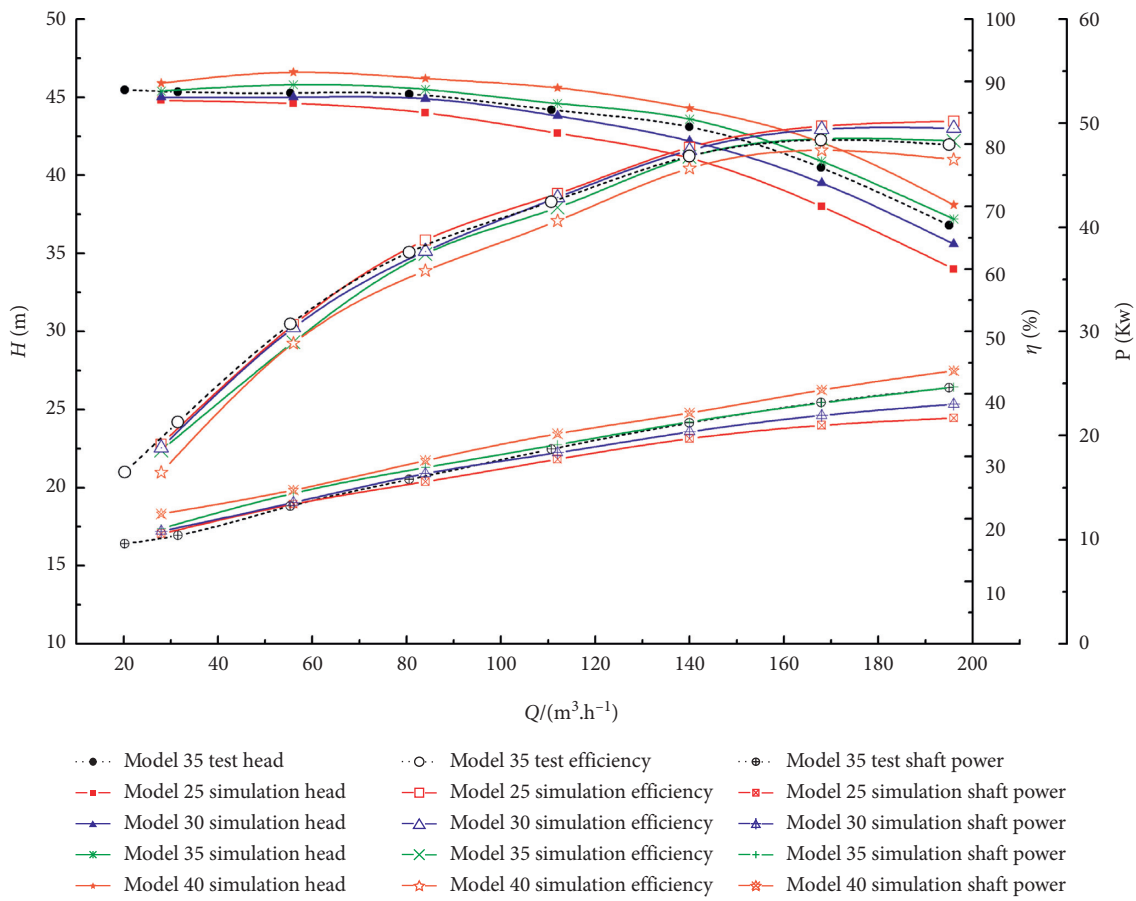

Figure 15: Experimental and numerical performance curves.

periodicity of the radial force and the sensitivity to the vibration of the pump unit, the acceleration sensor is arranged at the connection between the volute and the connecting body, as shown in Figure 16. The vibration sensor used in the test is INV9832 acceleration sensor, and the noise signal is collected by INV3020 series high performance 24 bit data acquisition system. The sampling frequency is 10 kHz and the sampling time is 60 s and is analyzed by DASP software.

The formula between vibration velocity and vibration intensity is as shown formula (3), where v_i is the vibration velocity of monitoring point (mm/s) and V_{rms} is the vibration intensity (mm/s). The vibration intensity indicates the severity of vibration, and it is expressed by the RMS of vibration velocity at the specified point. The results of vibration intensity test on the prototypes of model 25 and model 35 are shown in Figure 17. It can be clearly seen that the vibration intensities of model 25 and model 35 are consistent with the changing trend with the flow. The vibration intensities of model 25 and model 35 are the largest at a small flow rate and decrease as the flow rate increases, which is consistent with the trend of the simulation analysis results of the radial force in the pump. At the flow rate of 0.8Q, 1.0Q, 1.2Q, and 1.4Q, the vibration intensities are less than 2.5 mm/s. The vibration intensity of model 25 is about 0.2 mm/s less than that of model 35 at the same flow rate,

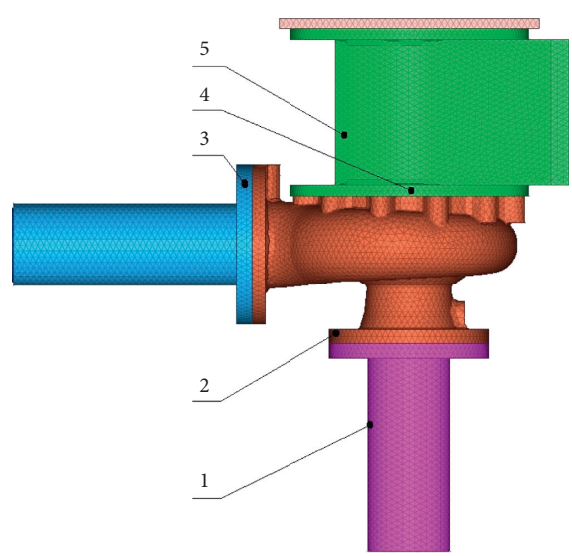

Figure 16: Schematic diagram of pump measuring point. 1. Inlet pipe. 2. Volute. 3. Outlet pipe. 4. Measuring point. 5. Connecting body.

which indicates that the blade outlet angle has a significant influence on the radial force of the pump and the vibration of the pump unit.

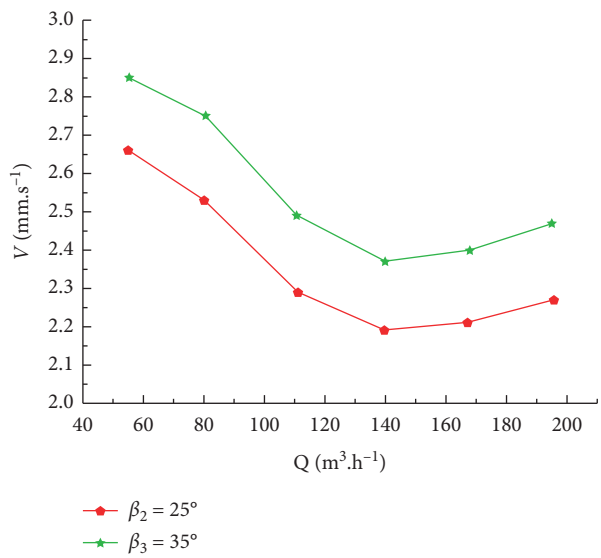

Figure 17: Vibration intensity test of the pump.

$$V_{\text{rms}} = \sqrt{\frac{1}{N}\sum_{i=1}^{N} v^2 i}. \quad (3)$$

6. Conclusions

(1) The main frequency of the radial resultant force on the impeller and the blades are the APF. There are peaks at the BPF and blade frequency multiplier. The main frequency of impeller torque fluctuation is the BPF. There are peaks at blade frequency multiplier, and the peak value gradually decreases.

(2) The radial forces of the impeller and the blades increase with the increase of the blade outlet angle at the same flow rate. With the same blade outlet angle, the radial forces decrease with the increase of the flow rate. The roundness of radial force vector diagram becomes more obvious with the decrease of the blade outlet angle.

(3) The RMS of radial resultant force on the blades is about 27%–33% of that on the impeller, which is mainly distributed around 30%.

(3) At the same flow rate, the main frequency and maximum fluctuation amplitudes on the impeller and the blades increase with the increase of the blade outlet angle. Meanwhile, the impeller torque increase with the increase of the blade outlet angle.

(4) With the same blade outlet angle, the main frequency, maximum fluctuation amplitudes, and the impeller torque decrease with the increase of the flow rate. The amplitude difference decreases with the increase of the flow rate.

(5) The blade outlet angle has an obvious greater influence on the radial force of the impeller and the blades under the small flow rate condition than other flow rate conditions.

(6) The simulation precision of model 35 pump head is controlled within 1.2% under the design flow rate condition, and the model can accurately simulate and predict the pump hydraulic performance.

(7) The vibration test of model 25 and model 35 prototype shows that the vibration intensities of the pump unit are less than 2.5 mm/s under 0.8Q, 1.0Q, 1.2Q, and 1.4Q flow rate conditions. The vibration intensity of model 25 is about 0.2 mm/s less than that of model 35.

Abbreviations

b_2: Impeller outlet width
d_h: Impeller hub diameter
D_1: Impeller inlet diameter
D_2: Impeller outlet diameter
D_3: Volute base circle diameter
e: Natural constant
F_b: RMS of radial force on the blades
F_i: RMS of radial force on the impeller
ΔF: Difference between the maximum and minimum values of the RMS
H: Pump head
p: Pressure
P: Shaft power
Q: Rated flow
n: Rotation
n_s: Specific speed
$N_{\max}$: Maximum value of the radial resultant force
$N_{\min}$: Minimum value of the radial resultant force
t: Time
$T_{\max}$: Maximum value of the impeller torque
$T_{\min}$: Minimum value of the impeller torque
v_i: Vibration velocity
V_{rms}: Vibration intensity
Z: Blade number
β_1: Blade inlet angle
β_2: Blade outlet angle
Φ: Blade wrap angle
φ: Tongue angle
ρ: Density
η: Pump efficiency
ω: Frequency.

Data Availability

The data used to support the findings of this study are included within the article.

Conflicts of Interest

The authors declare that they have no conflicts of interest.

Authors' Contributions

Fan-yu KONG was in charge of the whole project, Hong-li ZHANG proposed the analysis methodology and wrote the manuscript, Ai-xia ZHU proofread the manuscript, and

Fei ZHAO and Zhen-fa XU assisted with laboratory analyses. All authors read and approved the final manuscript.

Acknowledgments

This project was supported by the National Natural Science Foundation of China (no. 11602097) and Scientific Research Project of Wuxi Institute of Technology, China (no. ZK201804).

References

[1] R. Dong, S. Chu, and J. Katz, "Effect of modification to tongue and impeller geometry on unsteady flow, pressure fluctuations, and noise in a centrifugal pump," *Journal of Turbomachinery*, vol. 119, no. 3, pp. 506–515, 1997.

[2] R. Barrio, J. Parrondo, and E. Blanco, "Numerical analysis of the unsteady flow in the near-tongue region in a volute-type centrifugal pump for different operating points," *Computers & Fluids*, vol. 39, no. 5, pp. 859–870, 2010.

[3] I. Chalghoum, S. Elaoud, H. Kanfoudi, and M. Akrout, "The effects of the rotor-stator interaction on unsteady pressure pulsation and radial force in a centrifugal pump," *Journal of Hydrodynamics*, vol. 30, no. 4, pp. 672–681, 2018.

[4] L. Zheng, H.-S. Dou, X. Chen, Z. Zhu, and B. Cui, "Pressure fluctuation generated by the interaction of blade and tongue," *Journal of Thermal Science*, vol. 27, no. 1, pp. 8–16, 2018.

[5] I. Chalghoum, H. Kanfoudi, S. Elaoud, M. Akrout, and R. Zgolli, "Numerical modeling of the flow inside a centrifugal pump: Influence of impeller-volute interaction on velocity and pressure fields," *Arabian Journal for Science and Engineering*, vol. 41, no. 11, pp. 4463–4476, 2016.

[6] R. Spence and J. Amaral-Teixeira, "Investigation into pressure pulsations in a centrifugal pump using numerical methods supported by industrial tests," *Computers & Fluids*, vol. 37, no. 6, pp. 690–704, 2008.

[7] L. Cao, Y. Xiao, Z. Wang, Y. Luo, and X. Zhao, "Pressure fluctuation characteristics in the sidewall gaps of a centrifugal dredging pump," *Engineering Computations*, vol. 34, no. 4, pp. 1054–1069, 2017.

[8] X. Li, B. Yu, Y. Ji, J. Lu, and S. Yuan, "Statistical characteristics of suction pressure signals for a centrifugal pump under cavitating conditions," *Journal of Thermal Science*, vol. 26, no. 1, pp. 47–53, 2017.

[9] V. L. Khitrik, "The effect of the liquid flow in the outlet of a centrifugal pump on the acoustic resonance," *Acoustical Physics*, vol. 51, no. 4, pp. 463–468, 2005.

[10] M. Binama, W.-T. Su, W.-H. Cai et al., "Blade trailing edge position influencing pump as turbine (PAT) pressure field under part-load conditions," *Renewable Energy*, vol. 136, pp. 33–47, 2019.

[11] S.-S. Yang, F.-Y. Kong, W.-M. Jiang, and X.-Y. Qu, "Effects of impeller trimming influencing pump as turbine," *Computers & Fluids*, vol. 67, no. 30, pp. 72–78, 2012.

[12] L. Guo, J. Liu, L. Wang, D. Qin, and X. Wei, "Pressure fluctuation propagation of a pump turbine at pump mode under low head condition," *Science China Technological Sciences*, vol. 57, no. 4, pp. 811–818, 2014.

[13] D. Li, R. Gong, H. Wang, G. Xiang, X. Wei, and Z. Liu, "Dynamic analysis on pressure fluctuation in vaneless region of a pump turbine," *Science China Technological Sciences*, vol. 58, no. 5, pp. 813–824, 2015.

[14] Z. Zou, F. Wang, Z. Yao, R. Tao, R. Xiao, and H. Li, "Impeller radial force evolution in a large double-suction centrifugal pump during startup at the shut-off condition," *Nuclear Engineering and Design*, vol. 310, pp. 410–417, 2016.

[15] W. Jiang, G. Li, P.-f. Liu, and L. Fu, "Numerical investigation of influence of the clocking effect on the unsteady pressure fluctuations and radial forces in the centrifugal pump with vaned diffuser," *International Communications in Heat and Mass Transfer*, vol. 71, pp. 164–171, 2016.

[16] W. G. Zhao, M. Y. He, C. X. Qi, and Y. B. Li, "Research on the effect of wear-ring clearances to the axial and radial force of a centrifugal pump," *IOP Conference Series: Materials Science and Engineering*, vol. 52, no. 7, Article ID 072015, 2013.

[17] H. Alemi, S. Ahmad Nourbakhsh, M. Raisee, and A. Farhad Najafi, "Development of new "multivolute casing" geometries for radial force reduction in centrifugal pumps," *Engineering Applications of Computational Fluid Mechanics*, vol. 9, no. 1, pp. 1–11, 2015.

[18] K. Wang, G. Luo, Y. Li, R. Xia, and H. Liu, "Multi-condition optimization and experimental verification of impeller for a marine centrifugal pump," *International Journal of Naval Architecture and Ocean Engineering*, vol. 12, pp. 71–84, 2020.

[19] H. Ding, Z. Li, X. Gong, and M. Li, "The influence of blade outlet angle on the performance of centrifugal pump with high specific speed," *Vacuum*, vol. 159, pp. 239–246, 2019.

[20] H. Yousefi, Y. Noorollahi, M. Tahani, R. Fahimi, and S. Saremian, "Numerical simulation for obtaining optimal impeller's blade parameters of a centrifugal pump for high-viscosity fluid pumping," *Sustainable Energy Technologies and Assessments*, vol. 34, pp. 16–26, 2019.

[21] W. Li, L. Ji, W. Shi, L. Zhou, H. Chang, and R. K. Agarwal, "Expansion of high efficiency region of wind energy centrifugal pump based on factorial experiment design and computational fluid dynamics," *Energies*, vol. 13, no. 2, p. 483, 2020.

[22] K. Wang, H. Liu, X. Zhou, and W. Wang, "Experimental research on pressure fluctuation and vibration in a mixed flow pump," *Journal of Mechanical Science and Technology*, vol. 30, no. 1, pp. 179–184, 2016.

[23] Y. Hao and L. Tan, "Symmetrical and unsymmetrical tip clearances on cavitation performance and radial force of a mixed flow pump as turbine at pump mode," *Renewable Energy*, vol. 127, pp. 368–376, 2018.

[24] C. Dai, F.-y. Kong, and L. Dong, "Pressure fluctuation and its influencing factors in circulating water pump," *Journal of Central South University*, vol. 20, no. 1, pp. 149–155, 2013.

[25] W. Li, E. Li, L. Ji, L. Zhou, W. Shi, and Y. Zhu, "Mechanism and propagation characteristics of rotating stall in a mixed-flow pump," *Renewable Energy*, vol. 153, pp. 74–92, 2020.

[26] L. Ji, W. Li, W. Shi, H. Chang, and Z. Yang, "Energy characteristics of mixed-flow pump under different tip clearances based on entropy production analysis," *Energy*, vol. 199, Article ID 117447, 2020.

[27] L. Zhou, W. Wang, J. Hang, W. Shi, H. Yan, and Y. Zhu, "Numerical investigation of a high-speed electrical submersible pump with different end clearances," *Water*, vol. 12, no. 4, p. 1116, 2020.

[28] L. Zhou, C. Han, L. Bai, W. Shi, and R. Agarwal, "Numerical and experimental study of multiphase transient core-annular flow patterns in a spouted bed," *ASME Journal of Energy Resource Technology*, vol. 142, no. 9, Article ID 092104, 2020.

[29] L. Zhou, K. Deshpande, X. Zhang, and R. K. Agarwal, "Process simulation of chemical looping combustion using ASPEN plus for a mixture of biomass and coal with various oxygen carriers," *Energy*, vol. 195, Article ID 116955, 2020.

[30] G. Peng, X. Huang, L. Zhou, G. Zhou, and H. Zhou, "Solid-liquid two-phase flow and wear analysis in a large-scale centrifugal slurry pump," *Engineering Failure Analysis*, vol. 114, Article ID 104602, 2020.